


Rapid High-fidelity Multiplexed Readout of Superconducting Qubits

Johannes Heinsoo,* Christian Kraglund Andersen, Ants Remm, Sebastian Krinner, Theodore Walter, Yves Salathé, Simone Gasparinetti, Jean-Claude Besse, Anton Potočnik, Andreas Wallraff, and Christopher Eichler

Department of Physics, ETH Zurich, CH-8093 Zurich, Switzerland

 (Received 7 March 2018; revised manuscript received 26 June 2018; published 20 September 2018)

The duration and fidelity of qubit readout are critical factors for applications in quantum-information processing as they limit the fidelity of algorithms which reuse qubits after measurement or apply feedback based on the measurement result. Here we present fast multiplexed readout of five qubits using a single 1.2-GHz-wide readout channel. Using a readout pulse length of 80 ns and populating readout resonators for less than 250 ns, we find an average probability of correct assignment for the five measured qubits to be 97%. The differences between the individual readout errors and those found when measuring the qubits simultaneously are within 1%. We employ individual Purcell filters for each readout resonator to suppress off-resonant driving, which we characterize by measuring the dephasing imposed on unintentionally measured qubits. We expect the readout scheme presented here to become particularly useful for the selective readout of individual qubits in multiqubit quantum processors.

DOI: [10.1103/PhysRevApplied.10.034040](https://doi.org/10.1103/PhysRevApplied.10.034040)

I. INTRODUCTION

An essential feature of any digital quantum computer or simulator is the ability to measure the state of multiple qubits with high fidelity. In particular, high-fidelity single-shot measurements are needed for determining the result of a quantum computation [1], for observing error syndromes in quantum error correction [2,3], and for achieving high channel capacity in quantum communication protocols such as quantum teleportation [4,5]. Moreover, quantum nondemolition measurements are used for conditioning quantum-state initialization [6–8]. Recent progress in scaling up quantum processors based on superconducting qubits has stimulated research towards multiplexed readout architectures with the goal of reducing device complexity and enhancing resource efficiency, as discussed in more detail below [9–11].

Superconducting qubits are most commonly measured by employing their off-resonant coupling to a readout resonator [12,13]. This dispersive interaction results in a qubit-state-dependent shift of the resonator frequency, which is probed using coherent microwave fields. Recent improvements in the efficiency of microwave parametric amplifiers [14–17] have enabled single-shot readout with high fidelity [18,19]. Furthermore, the use of Purcell filters [11,20,21] led to the implementation of faster readout circuits resulting in a reduction of the readout time down to 50 ns for a single qubit without introducing additional qubit decay [22].

Extensions of dispersive readout to multiple qubits can be realized by either coupling multiple qubits to a single readout resonator [23,24] or by probing several readout resonators coupled to a single feedline with a multifrequency pulse [9]. The latter approach allows for selective readout of any subset of the qubits by choosing the corresponding frequency components in the measurement pulse. High-fidelity frequency-multiplexed readout was first achieved with multiple bifurcation amplifiers [10], one for each qubit, and more recently by employing a single broadband parametric amplifier [11,25–27]. Multiplexed readout with Purcell protection has been achieved by coupling multiple readout resonators to a single resonator-based Purcell filter [28]. Broadband Purcell filters based on stepped impedance resonators have also been realized [21]. Other recent multiqubit experiments either employ individual readout lines for each qubit [29,30] or avoid Purcell decay of qubits by using narrowband readout resonators [28,31–34], which, however, increase the time required for high-fidelity qubit readout.

In this work, we demonstrate frequency-multiplexed readout of up to five qubits using a single readout channel, see Fig. 1(a) for a schematic of the concept. We use individual Purcell filters for each readout resonator, which in addition to protecting the qubits from Purcell decay, also suppress the off-resonant driving of untargeted readout resonators, thus avoiding the unintentional dephasing of qubits. We characterize this readout crosstalk in our experiments, by analyzing correlations in the readout between all pairs of qubits and by measuring the additional dephasing imposed on untargeted qubits during the readout.

*jheinsoo@phys.ethz.ch

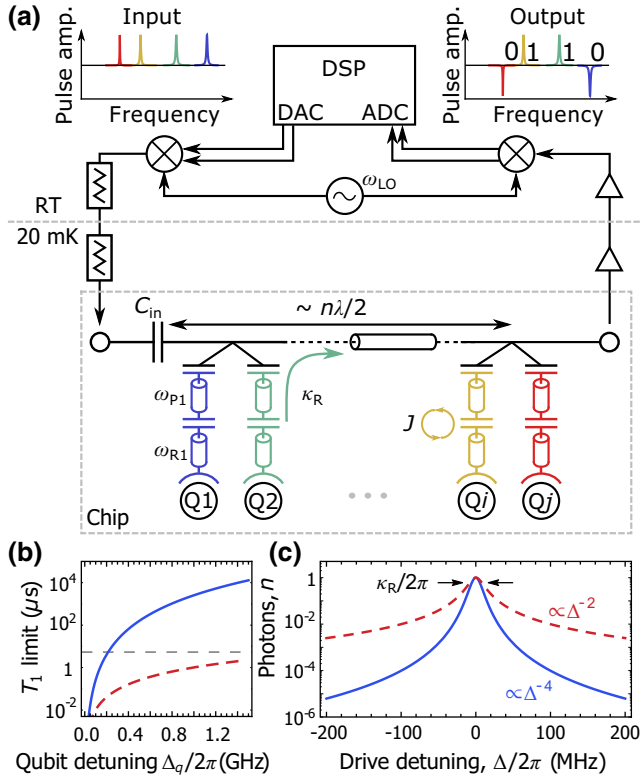


FIG. 1. (a) Schematic of the multiplexed readout experiment showing a circuit diagram of the superconducting chip at $T \approx 20$ mK and the room-temperature (RT) electronics. Multifrequency pulses used for readout are synthesized with a digital signal processing (DSP) unit, then up-converted to microwave frequencies by analog mixing with a local oscillator (LO) field, and applied to the input port of the feedline after several stages of attenuation. The readout signal emitted from the sample is amplified, down-converted, and digitized with an analog-to-digital converter (ADC) and further processed with the same DSP unit used for pulse synthesis. (b) Qubit lifetime T_1 limited by the Purcell effect vs detuning between the readout qubit and readout resonator Δ_q with (blue solid line) and without (red dashed line) Purcell filter. The dashed gray horizontal line at $T_1 = 5 \mu\text{s}$ indicates typical T_1 times measured in this work. (c) Calculated photon number in the readout resonator with $\kappa_R/2\pi = 20$ MHz normalized to its maximum value as a function of drive detuning $\Delta = \omega_d - \omega_R$ with (blue solid line) and without (red dashed line) Purcell filter.

The presented multiplexed readout concept is expected to be particularly useful in multiqubit algorithms, in which subsets of qubits are measured while other qubits evolve coherently. In the surface code [35], for example, a set of ancillary qubits is repeatedly measured while keeping all data qubits ideally unperturbed. Other examples for protocols relying on readout of individual qubits during the algorithm include the iterative quantum Fourier transform [36], entanglement distillation [37], and deterministic entanglement swapping [38].

II. CONCEPT OF READOUT ARCHITECTURE

For readout we dispersively couple each qubit Q_i to a resonator R_i with resonance frequency ω_{R_i} , see Fig. 1(a). The readout resonator is coupled through a dedicated Purcell filter P_i to a common feedline. The effective linewidth of the readout resonator is given by

$$\kappa_R = \frac{1}{2} \left(\kappa_P - \text{Re} \left\{ \sqrt{-16J^2 + (\kappa_P - 2i\Delta_{RP})^2} \right\} \right), \quad (1)$$

with the linewidth of the Purcell filter κ_P , the coupling strength J and detuning between readout resonator and Purcell filter $\Delta_{RP} = \omega_R - \omega_P$, see Appendix C for details. In order to achieve fast readout we targeted an effective linewidth of $\kappa_R/2\pi \gtrsim 10$ MHz. Taking a realistic detuning of $\Delta_{RP}/2\pi \lesssim 5$ MHz into account, which results from the finite accuracy of circuit design and fabrication, we design $J/2\pi = 10$ MHz and $\kappa_P/2\pi = 40$ MHz to approach our targeted κ_R . Furthermore, the Purcell filter parameters are designed to strongly suppress qubit decay into the feedline [20,39]. As illustrated in Fig. 1(b), for detunings $\Delta_q = \omega_Q - \omega_R > 0.6$ GHz between qubit and resonator the T_1 limit imposed by Purcell decay through the readout resonator is well above the state-of-the-art qubit lifetimes. Also, the typical T_1 times measured in our current device are above the Purcell limit of a directly coupled readout resonator with the same κ_R indicating that Purcell filters are necessary to achieve the targeted readout parameters without degrading the qubit performance.

All Purcell filters are coupled to a common feedline and have an approximately equal frequency spacing of $\Delta_R/2\pi \approx 160$ MHz. Choosing this relatively small frequency spacing in combination with a large κ_R , could induce significant population in untargeted resonators while driving another resonator nearby in frequency. Such an unintentional resonator population causes additional dephasing of untargeted qubits [40]. The use of dedicated Purcell filters, however, strongly suppresses the off-resonant driving of each individual readout resonator. In the limit of large drive detuning the intracavity photon number scales as $\propto \Delta^{-4}$ with a Purcell filter, as compared to $\propto \Delta^{-2}$ without it, see Fig. 1(c).

We synthesize a multifrequency probe pulse using a digital signal processing (DSP) unit and then upconvert, attenuate, and apply the pulse to the input port of the feedline. A capacitor C_{in} at the input provides directionality to the readout signal, which preferentially decays from the resonator towards the output port and thus minimizes signal loss into the input port. For the chosen capacitance of $C_{in} = 40$ fF, a proportion of $(1 + |\Gamma|^2)/2 \approx 98\%$ of the readout signal propagates towards the output port, where $\Gamma(\omega) = 1/(1 + 2i\omega Z_0 C_{in})$ is the reflection coefficient of the capacitor, see Appendix C for details. Moreover, due to the vanishing current across the input capacitor C_{in} , the environmental impedance seen by the Purcell filter

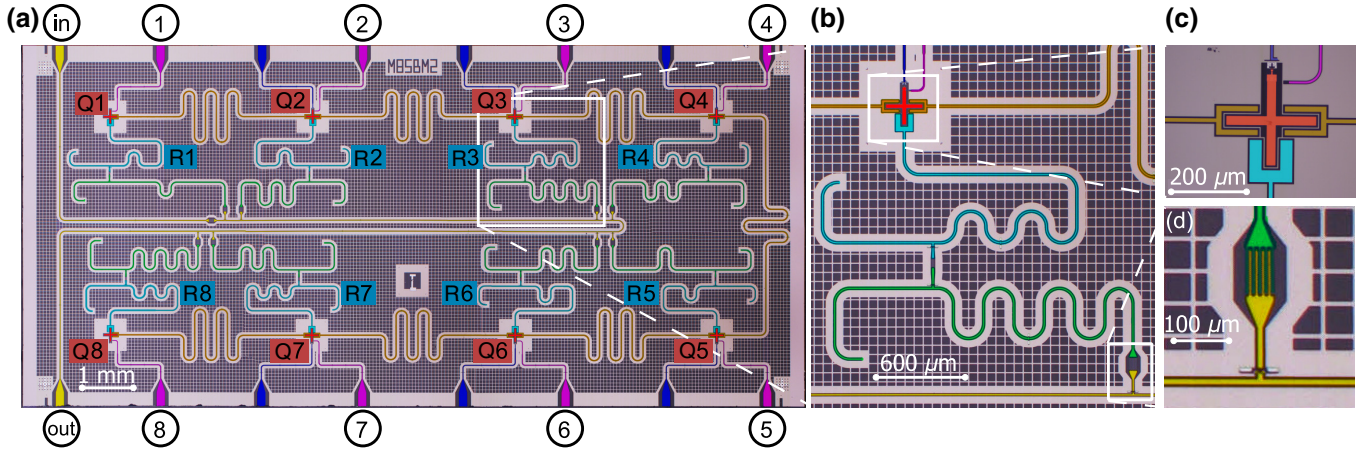


FIG. 2. (a) False-colored optical micrograph of the device with qubits Q_i (red), readout resonators R_i (blue), Purcell filters (green), coupling resonators (orange), charge lines for single-qubit manipulation (purple), flux lines for single-qubit tuning (dark blue), and a common feedline (yellow). The ports used for probing the device are denoted in circles. (b) Enlarged view of Q_3 with its readout resonator and Purcell filter. (c) Cross-shaped single-island flux-tunable transmon qubit inductively coupled to a flux line, capacitively coupled to a readout resonator, two coupling resonators, and a charge line. (d) Interdigitated capacitor between the Purcell filter and the feedline.

depends on both its distance from the input capacitor and its frequency. For maximum coupling we place the Purcell filters at distances from the capacitor, which are close to integer multiples of half the wavelength of the resonator field $n\lambda_{R_i}/2$.

The output signal emitted from the sample is amplified by a traveling-wave parametric amplifier (TWPA), which is a broadband near-quantum-limited nondegenerate amplifier with an average gain of 20 dB in the relevant bandwidth 6.5–7.8 GHz and a compression point of $P_{1\text{ dB}} = -100$ dBm [26]. After several additional stages of amplification (see Appendix A) the readout signal is downconverted and digitized with the same DSP unit as used for pulse synthesis. As the DSP unit has a total bandwidth of 1.2 GHz we can, in principle, read out the state of up to eight qubits given our choice of frequency spacing Δ_R . The firmware version of our DSP unit used in this experiment, however, limits us to simultaneous readout of only five qubits. The digitized signal is filtered in parallel for each readout frequency with a mode-matched filter implemented by weighted integration. The combination of an asymmetric feedline, a near-quantum-limited amplifier, and mode-matched filtering results in a total average measurement efficiency of $\eta = 49\%$, which we define as the squared ratio of the achieved and the quantum-limited signal-to-noise ratio (SNR), see Appendix F.

III. DEVICE DESCRIPTION AND CHARACTERIZATION

We demonstrate the concept described above, with a device featuring eight single-island flux-tunable transmon qubits [41,42], see Fig. 2. Each qubit has an individual

drive line to perform single-qubit gates and a flux line for frequency tuning except qubits Q_1 and Q_8 , which are tuned using superconducting coils mounted below the sample holder. All the following experiments are realized using qubits 2, 3, 5, 6, and 7; compare Fig. 2. While the readout resonators and Purcell filters are implemented as $\lambda/4$ resonators, qubit-qubit coupling resonators are realized as $\lambda/2$ resonators. The planar Nb and Al structures on the sapphire substrate of the device are defined using photo- and e-beam lithography; for fabrication details see Appendix B.

Transmission spectra measured from the eight qubit drive lines to the output port reveal a single peak for each readout resonator, see Fig. 3(a). The frequency spacing between individual resonator frequencies is close to the designed value of 160 MHz. We extract linewidths $\kappa_{R_i}/2\pi$ between 3 and 11 MHz. We attribute additional features in the measured spectra to the residual direct coupling between the drive lines to other elements on the chip, as well as the finite detuning between the readout resonators and their corresponding Purcell filters.

We measure the state-dependent dispersive shift χ for each qubit by preparing either the ground or excited state before probing the transmission from the input to the output port of the feedline, see Fig. 3(b) for example data for Q_6 . We observe a wide dip in the transmission spectrum resulting from the Purcell filter and an additional peak in the center close to the frequency of the readout resonator. The frequency of this peak depends on the qubit state while the background, dominated by the Purcell filter response, remains largely unaffected. The measured transmission data around a single resonance is well reproduced by the analytic expression obtained from the input-output theory, see Appendix C. From fits of this model to all

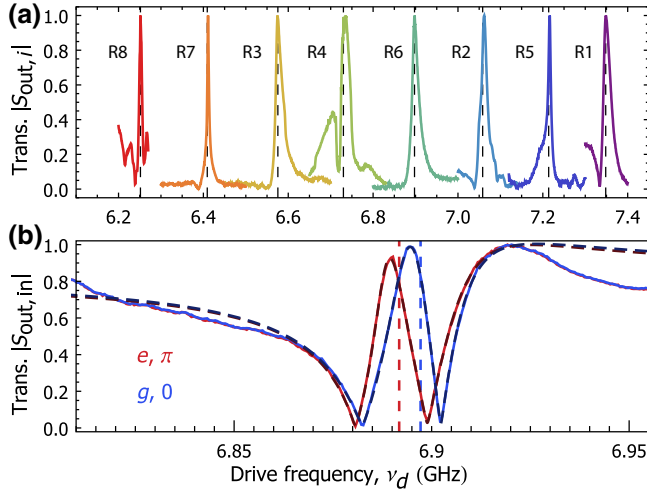


FIG. 3. (a) Transmission spectra $|S_{\text{out},i}(\nu_d)|$ of the readout resonators normalized to their respective maximum values measured from the charge line ports i to the feedline output port as a function of drive frequency ν_d with resonance frequencies (dashed vertical lines) obtained from Lorentzian fits. (b) Transmission spectrum $|S_{\text{out},\text{in}}(\nu_d)|$ measured from the feedline input to the output port close to the resonance frequency of R6 with (red line) and without (blue line) a π pulse applied to qubit Q6 prior to measurement. The dashed lines are fits to the model described in Appendix C with vertical dashed lines indicating the fitted readout resonator frequencies for the two cases.

measured data sets we obtain the resonator parameters summarized in Table I. The effective linewidths and dispersive shifts of most qubits are smaller than the target values discussed in Sec. II. owing to imprecisions in device fabrication. To achieve detunings Δ_{RP} between the readout resonator and Purcell filter below 20 MHz across the entire sample we carefully modeled the microwave properties of the individual elements, as discussed in Appendix D.

We perform time-resolved measurements of the resonator response to a 80-ns-long probe pulse for the qubit initially prepared in either the ground or excited state, see Fig. 4. We show the measured response downconverted by

TABLE I. Parameters of readout resonator R_i obtained from fits to transmission spectra equivalent to the one shown in Fig. 3(b). The Purcell filter frequency ω_P , readout resonator frequency ω_R , Purcell filter linewidth κ_P , and their coupling rate J , the effective readout resonator linewidth κ_R , and dispersive shift χ are listed.

	R2	R3	R5	R6	R7
$\omega_R/2\pi$ (GHz)	7.058	6.575	7.214	6.898	6.409
$\omega_P/2\pi$ (GHz)	7.057	6.580	7.196	6.898	6.392
$\kappa_P/2\pi$ (MHz)	32.2	35.6	57.8	38.3	32.6
$J/2\pi$ (MHz)	9.2	7.9	6.9	8.7	7.8
$\kappa_R/2\pi$ (MHz)	14.3	7.8	4.5	11.3	3.1
$\chi/2\pi$ (MHz)	-4.05	-1.11	-4.80	-2.66	-1.92

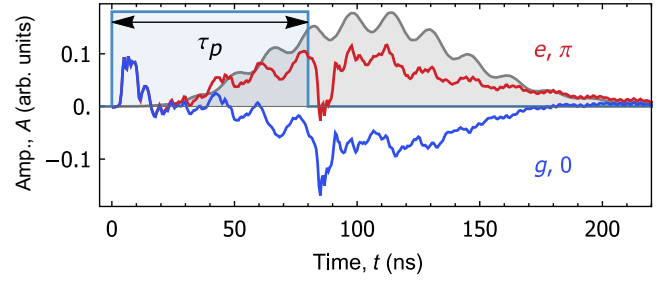


FIG. 4. Measured quadrature amplitude A as a function of time t when applying a square pulse (light blue) of length $\tau_p = 80$ ns resonant with R6 and for the qubit Q6 prepared in the excited (red) and ground (blue) state and the difference of the two (gray).

the frequency of the probe pulse and present the amplitude A in the quadrature for which the integrated difference between the ground and excited state response is maximal. At the start and the end of the readout pulse we observe a peak and a dip, respectively, which are both independent of the qubit state. We attribute this feature to the fast ring-up and ring-down dynamics of the Purcell filter. Other sharp features are due to spurious qubit-state-independent high-frequency components in the broadband measurement signal. The smooth change in the difference between the ground and excited state responses (gray line) stems from the qubit-resonator dynamics. Oscillations in the signals and their difference result from a two-frequency beating caused by the finite quadrature imbalance of the downconversion mixer.

We measure the difference between the ground and excited state response of all readout resonators, the complex conjugate of which we use as the integration weights in the DSP unit. Choosing this quantity as a mode-matched filter is known to provide near-optimal filter efficiency for a given readout frequency and power [43,44].

IV. MULTIPLEXED SINGLE-SHOT READOUT

We quantify the performance of single-shot readout for each qubit by preparing the qubit in either the ground or the excited state and by subsequently applying a readout pulse at the corresponding readout resonator frequency. The integrated response signal s for the two input states follows a bimodal Gaussian distribution with the distribution width σ as shown in Fig. 5 for qubits Q2 and Q6 having the smallest and largest $\text{SNR} = (\langle s \rangle_\pi - \langle s \rangle_0) / \sigma$. We normalize s by the width of the distribution σ to make the SNR easily comparable for the different qubits. Each qubit state is prepared $n_{\text{rep}} \approx 1.3 \times 10^6$ times. In all experiments we also apply an additional readout pulse prior to the state preparation to herald the ground state [6,7,22]. The heralding discards $P_{\text{therm}} = 4\text{--}6\%$ of the experiments for each qubit corresponding to the probability for the qubit to be thermally excited [45].

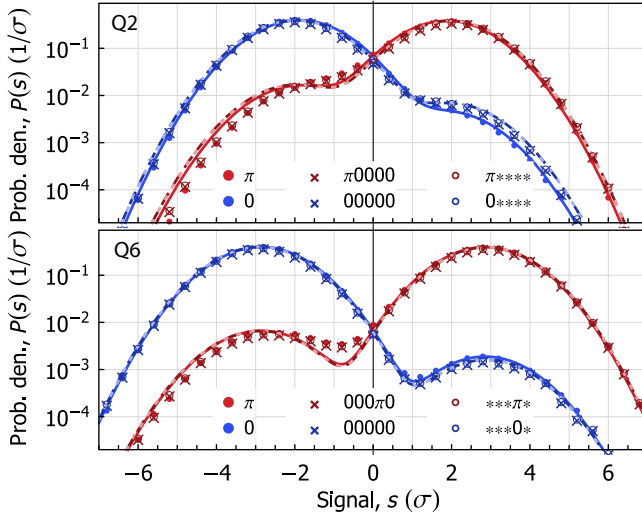


FIG. 5. Histograms of integrated single-shot readout signal of Q2 and Q6, respectively, prepared with a π pulse (red) and without (blue). The signal s is normalized by the width of the Gaussian distribution. Experimental data (points) are shown with fits to a double Gaussian distribution (solid lines). Results from the individual readout experiment (\bullet) are compared to the case in which the readout pulse is also applied to all other qubits initially prepared in either a ground state (darker shade, \times) or averaged over all possible input states (brighter shade, \circ).

In order to assign a binary value corresponding to the outcome of the qubit measurement from the continuous valued signal s , we choose an assignment threshold, which best separates the prepared states of the qubit. We quantify the fidelity of the readout by the probability of correct assignment $P_c = [P(g|0) + P(e|\pi)]/2$, where π (0) marks the state preparation with (without) a π pulse, and e (g) represents an assignment to the excited (ground) state. We maximize P_c by optimizing the readout power and frequency for a given readout pulse length for each qubit individually.

The bimodal Gaussian fits to the single-shot histograms provide information on the sources of readout error [22]. There are three main error mechanisms: First, due to finite SNR, the two states cannot be fully distinguished because of the overlap of the two Gaussians. The overlap error accounts for less than 0.5% error probability for qubits Q3, 5, 6, and 7. For Q2 this error amounts to 3.1% owing to the lower readout power used for this qubit compared to all others. Second, qubit state mixing between the ground and excited states due to the readout tone [46] and rethermalization causes an error with probability $P(e|0) = 0.3\text{--}1.2\%$. Finally, when prepared in the excited state, the qubit may decay before or during the readout, which accounts for the remainder of the observed errors and ranges from 0.7% for Q3 to 5.5% for Q5 which has a combination of a slow readout resonator and low T_1

TABLE II. Probability of correct assignment P_{c1} and P_{c5} of the single qubit and simultaneous five-qubit single-shot readout correspondingly.

	Q2	Q3	Q5	Q6	Q7
P_{c1}	94.2%	98.8%	93.6%	97.9%	97.8%
P_{c5}	94.5%	98.8%	92.9%	98.6%	97.9%

compared to the other qubits, see Appendix B for a comparison of parameters. Overall, qubit decay appears to be the dominant source of error, which suggests that significant improvements in the readout performance are possible in future devices featuring longer T_1 times.

We repeat the single-shot readout experiment with probe pulses applied at all five readout frequencies simultaneously and with the qubits prepared in all $2^5 = 32$ combinations of basis states. From this dataset we first pick a subset, where all but one qubit are left in the ground state. The histograms with a single (dots) and multiqubit probe tone (crosses) are practically indistinguishable, see Fig. 5. This indicates that the probe tones do not have a significant spectral overlap with the mode-matched filters of the other qubits. Moreover, the signal distributions, obtained after averaging over all possible states of the other qubits (circles) are also almost identical. Thus, each frequency component contains information about a single qubit only, which is confirmed by the nearly identical probability of correct assignment for the individual readout P_{c1} and five-qubit readout P_{c5} shown in Table II. The remaining discrepancy is on the level of variation of P_c in repeated experiments.

As the readout performance for each qubit remains largely undisturbed by the additional readout tones we use the individually obtained assignment threshold values and mode-matched filter coefficients. The ability to independently calibrate each subsystem is desired for system scalability.

The probability matrix $P(s_1 \cdots s_5 | \zeta_1 \cdots \zeta_5)$ (Fig. 6) of assigning state $s_i \in \{g, e\}$ for preparation $\zeta_i \in \{0, \pi\}$ describes all state assignment. Ideally, $P(s|\zeta)$ is an identity matrix. The matrix obtained from the experimental data is close to diagonal with the largest deviation corresponding to assigning all qubits to the prepared excited states $P(eeeee|\pi\pi\pi\pi\pi) = 83.3\%$ as this input state is most susceptible to individual qubit decay. Apparent features in the full assignment probability matrix are the additional off-diagonal lines, which below the diagonal are indicative of individual qubit decay and above the diagonal of measurement-induced excitation during the measurement. These off-diagonal elements are most pronounced for Q2 and Q5, which have the largest decay and mixing errors. Moreover, as discussed in Appendix E, the cross correlations extracted from the assignment probability matrix are

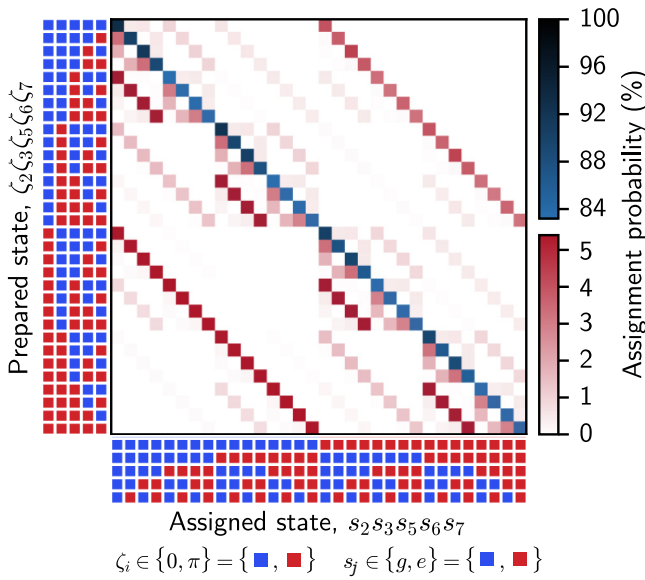


FIG. 6. Assignment probability matrix $P(s|\zeta)$ for each qubit Q_i prepared with a π pulse $\zeta_i = \pi$ (red) or without a pulse $\zeta_i = 0$ (blue) and each qubit assigned to either ground state $s_i = g$ (blue) or excited state $s_i = e$ (red). The qubits are ordered as Q2, Q3, Q5, Q6, and Q7 from left to right (top to bottom) for the prepared (assigned) state.

up to 0.3%, which is small compared to the single-qubit readout errors.

V. EFFECT OF MEASUREMENT CROSSTALK ON UNTARGETED QUBITS

As the readout resonators are coupled to a common feedline and have a finite spectral overlap, the readout

tone of qubit Q_j also populates the readout resonators of untargeted qubit Q_i with a qubit state-dependent field amplitude b_s , which causes parasitic measurement-induced dephasing [40]. While the instantaneous measurement-induced dephasing rate $\Gamma(t) = 2\chi \text{Im}[b_g(t)b_e^*(t)]$ changes during the measurement, the error per readout operation corresponds to the integrated effect of the probe pulse. Thus, we quantify the effect of measurement crosstalk on untargeted qubits as the average dephasing rate $\bar{\Gamma}_{ij} = (1/\tau_p) \int_0^\infty \Gamma_{ij}(t) dt$ of Q_i due to the measurement of Q_j with a pulse length τ_p .

We measure the average dephasing rate in a Ramsey experiment [44,47] with a fixed time between the Ramsey pulses, see the pulse scheme shown in the inset of Fig. 7(a). By varying the phase ϕ of the second $\pi/2$ pulse on Q_i we observe Ramsey oscillations with a contrast c . In between the $\pi/2$ pulses, we apply a probe pulse scaled in amplitude by a factor ξ relative to the final probe pulse. As shown for the example data in Fig. 7(a) for $i = 7$ and $j = 3$, the Ramsey contrast c decreases with increasing ξ . We fit the observed data to the expression $c(\xi) = c_0 e^{-\bar{\Gamma}\tau_p\xi^2}$ to extract the measurement-induced dephasing rate $\bar{\Gamma}$. Here, the constant prefactor c_0 accounts for all other dephasing mechanisms which are independent of ξ .

When we apply the measurement pulse to the same qubit as the Ramsey experiment ($i = j$) we observe the intended measurement-induced dephasing. As discussed in Appendix F, the measured $\bar{\Gamma}_{ii}$ in combination with the SNR obtained from the histograms in Fig. 5 allows us to estimate the measurement efficiency η [44], which we find to be 42–52%, mostly limited by the dissipative components before the TWPA and the internal loss of the TWPA.

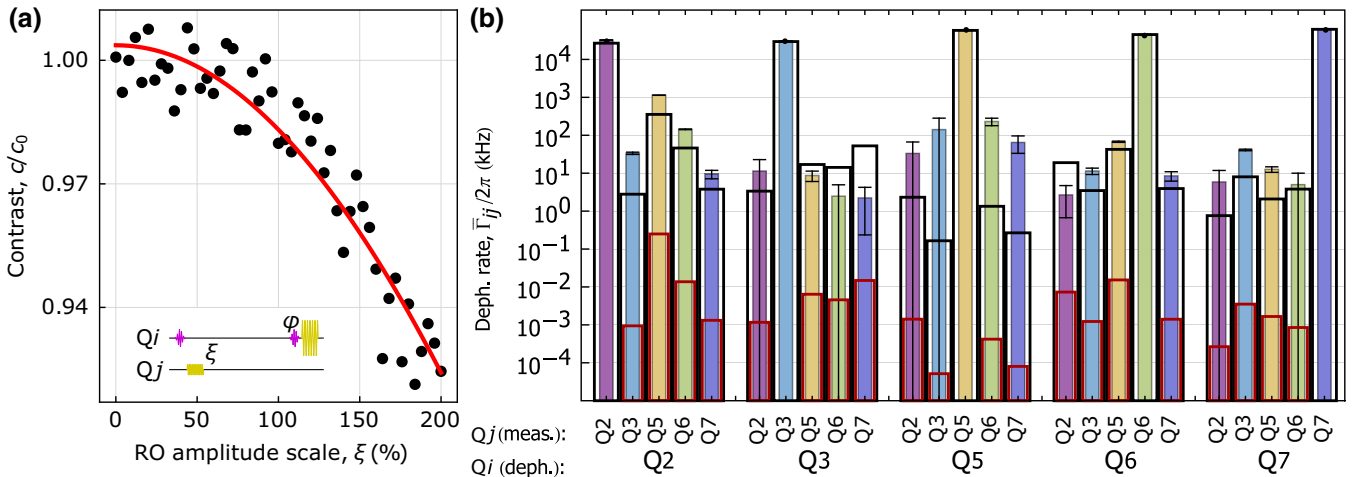


FIG. 7. (a) Contrast of the Ramsey oscillations c of qubit Q_7 as for different readout pulse amplitudes ξ relative to the final readout amplitude on Q_3 (dots) and a Gaussian fit (red line). (Inset) Pulse scheme used for the dephasing measurement consisting of 10-ns $\pi/2$ pulses (pink) and 80-ns readout pulses (yellow). (b) The average dephasing rate of qubit Q_i when applying a readout pulse to qubit Q_j . Experimentally measured rates (filled bars), calculated values based on the parameters extracted from the spectroscopy shown in Table I (black frames), and calculated dephasing rates for a Gaussian-filtered probe pulse (red frames).

TABLE III. Qubit and resonator properties obtained by methods described in the main text and Appendix B. Numbers in parentheses are the settings used for the dephasing measurements in Sec. V.

	Q2	Q3	Q5	Q6	Q7
Qubit frequency, $\omega_Q/2\pi$ (GHz)	6.254	5.206	6.441 (5.457)	5.902	5.442
Max. qubit frequency, $\omega_{Q,\max}/2\pi$ (GHz)	6.260	5.216	6.996	5.996	5.442
Qubit anharmonicity, $\alpha/2\pi$ (MHz)	-226	-246	-198	-234	-238
Qubit lifetime, T_1 (μ s)	5.7	6.0	4.9	5.8	5.8
Qubit coherence time, T_2^* (μ s)	4.1	2.5	0.7	3.1	7.8
Thermal population, P_{therm} (%)	4.7	5.1	2.9	6.0	6.4
Readout resonator frequency, $\omega_R/2\pi$ (GHz)	7.058	6.575	7.214 (7.200)	6.898	6.409
Purcell filter frequency, $\omega_P/2\pi$ (GHz)	7.057	6.580	7.196	6.898	6.392
Purcell filter linewidth, $\kappa_P/2\pi$ (MHz)	32.2	35.6	57.8	38.3	32.6
Readout-Purcell coupling, $J/2\pi$ (MHz)	9.2	7.9	6.9	8.7	7.8
Effective readout linewidth, $\kappa_R/2\pi$ (MHz)	14.3	7.8	4.5 (11.8)	11.3	3.1
Qubit coupling to R_i , $g/2\pi$ (MHz)	122.3	123.4	134.0	115.9	108.2
Dispersive shift, $\chi/2\pi$ (MHz)	-4.1	-1.7	-4.8 (-0.9)	-2.6	-2.4
Readout frequency, $\omega_{RO}/2\pi$ (GHz)	7.056	6.572	7.208	6.891	6.407
Readout IF, $\nu_{RO \text{ mod}}$ (MHz)	195	-289	347	30	-454
Readout photons, n_{RO}	4.1 (4.7)	22.2 (36.3)	2.9 (126)	5.8 (14.3)	9.7 (31.1)
Critical photons, n_{crit}	10.8	30.2	8.2 (42)	18.2	19.9

The parasitic measurement-induced dephasing $\bar{\Gamma}_{ij}$ ($i \neq j$) spans two orders of magnitude (Fig. 7). For example, the large dephasing of Q2 when measuring Q5 leads to a phase-error probability due to measurement-induced dephasing of $P_\phi = [1 - \exp(-\bar{\Gamma}_{ij} \tau_p)]/2 \approx 11\%$ while for other qubit pairs the corresponding phase-error probability is below 0.1%.

To calculate the expected dephasing rate for the sample parameters given in Appendix B, we solve for the field amplitude $b(t)$ in the readout resonator described by the equations of motion given in Appendix C. The comparison of the calculated, depicted with a black frame in Fig. 7, and the measured dephasing, depicted with filled bars, shows a qualitative agreement except for the dephasing of Q5, for which we did not obtain reliable data due to qubit-frequency instability and short dephasing time, see also Appendix B.

The good agreement with the model of parasitic measurement-induced dephasing justifies using the model for explaining the qualitative features and predicting possible future improvements. For example, Q2 is most strongly dephased by the measurement tones in R5 and R6 as these are the readout resonators closest in frequency to R2. The readout pulse for R5 dephases Q2 more strongly compared to the pulse for R6, since a much stronger tone is used for R5 due to its small dispersive shift χ_5 . In addition, Q2 shows the largest measurement-induced dephasing in general, as it has the largest χ and one of the largest κ_R which leads to the largest spectral overlap with the probe pulses targeted to other readout resonators. For the dephasing experiment presented here, Q5 is in a different configuration than for the experiments of the previous sections, as shown in Table III.

As the spectral overlap between the readout resonators is already small, the readout crosstalk is limited by the spectral width of the square-shaped probe pulses, which are significantly wider in spectrum than the readout resonators. As shown with red frames in Fig. 7, by convolving the pulse shape with a Gaussian kernel with a width $\sigma = 5$ ns, the parasitic measurement-induced dephasing could possibly decrease by 2–3 orders of magnitude; however, this prediction is not experimentally verified. For the same κ_R/Δ_R ratio, but without individual Purcell filters, such probe-pulse shaping would result in only a minor improvement.

VI. DISCUSSION AND OUTLOOK

In this work we demonstrate frequency multiplexed readout of five qubits with high qubit selectivity. We show that the presented architecture enables fast readout in combination with low crosstalk. In particular, the single-qubit readout performance remains unaffected by the presence of multiple readout tones at a level where the individual readout calibration can be used for multiqubit readout without degrading performance.

The primary source of errors in the single-shot qubit readout is single-qubit decay except Q2, for which the effect of measurement induced mixing is dominant. Furthermore, the main source of readout crosstalk arises from the probe pulses spanning to the resonance of untargeted readout resonators. From simulations we expect that a significant reduction of parasitic resonator population could be achieved by a Gaussian filtering of the pulses.

Due to the short readout resonator occupation time of 250 ns and potentially low crosstalk, the readout architecture presented in this work seems particularly suited

for quantum error-correction algorithms, in which a set of ancilla qubits is repeatedly measured while preserving the coherence of data qubits on the same chip [48].

ACKNOWLEDGMENTS

The authors thank Philipp Kurpiers, Paul Magnard, Simon Storz, Adrian Beckert, and Jacob Koenig for contributions to the experimental setup and Stefania Balasiu for contributions to the measurement control and analysis software. Moreover, the authors thank William D. Oliver for providing the TWPA.

The authors acknowledge financial support by the Office of the Director of National Intelligence (ODNI), Intelligence Advanced Research Projects Activity (IARPA), via the U.S. Army Research Office Grant No. W911NF-16-1-0071, by the National Centre of Competence in Research Quantum Science and Technology (NCCR QSIT), a research instrument of the Swiss National Science Foundation (SNSF) and by ETH Zurich.

The views and conclusions contained herein are those of the authors and should not be interpreted as necessarily

representing the official policies or endorsements, either expressed or implied, of the ODNI, IARPA, or the U.S. Government.

APPENDIX A: EXPERIMENTAL SETUP

We realize the experiments presented in the main text using the measurement setup depicted in Fig. 8. Here, the readout pulses are generated and detected with a sampling rate 1.8 gigasamples per second using a single ultrahigh-frequency lock-in amplifier (UHFLI) by Zurich Instruments. The AWG component of the built-in FPGA outputs a probe-pulse, which is up-converted to microwave frequencies using an IQ mixer, and routed to the sample through a chain of 20-dB attenuators thermally anchored at the 4 K, 100 mK, and 12 mK of a dilution refrigerator.

The weak measurement signal from the output of the sample is amplified using a wide bandwidth near-quantum-limited traveling wave parametric amplifier (TWPA) [26]. We connect the TWPA to wideband (3–12 GHz) isolators at its input and output to achieve appropriate impedance matching over the entire band of amplification. The pump

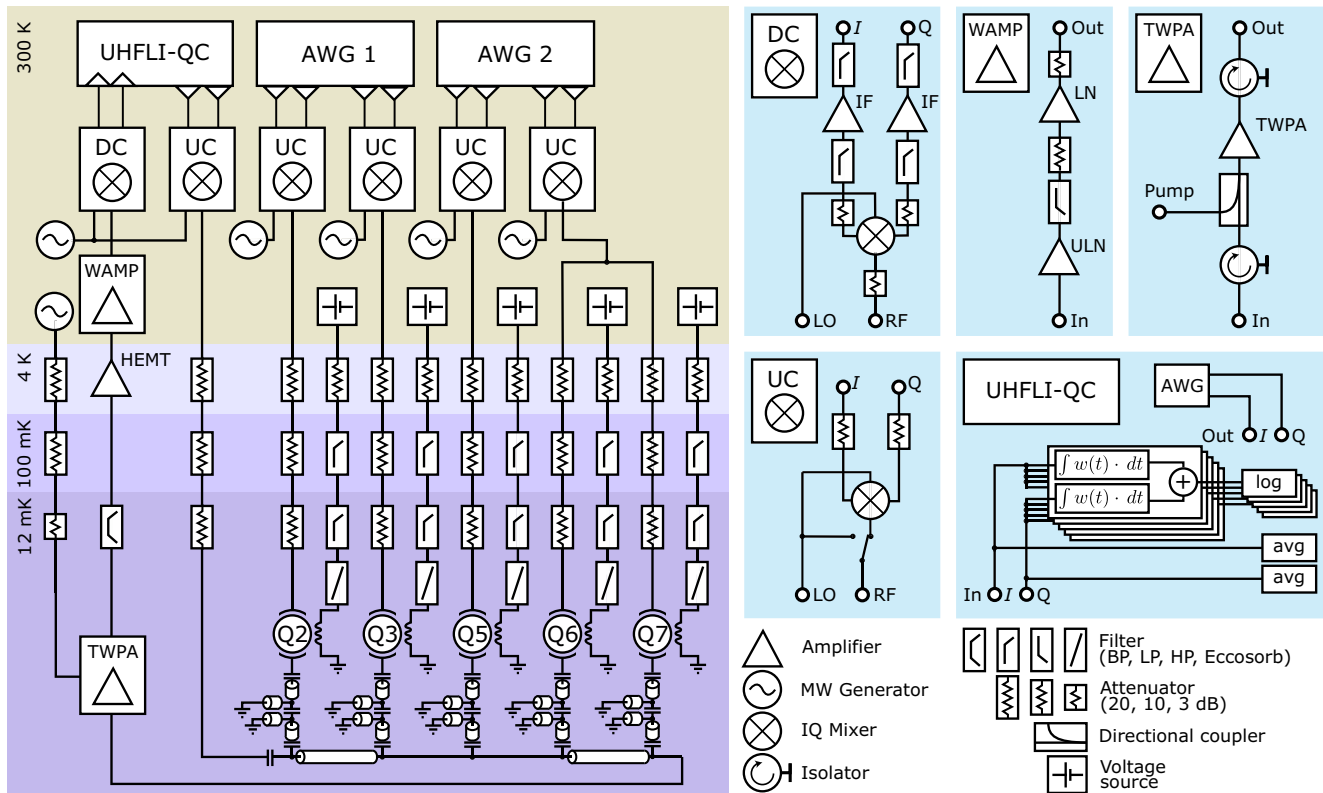


FIG. 8. Detailed schematic of the measurement setup. The colored background on the left side indicates the different temperature stages for the components. In the panels on the right we describe in more detail down-conversion (DC), up-conversion (UP), warm amplification (WAMP) boards, components used around traveling waveguide parametric amplifier (TWPA) and virtual hardware components of the Zurich Instruments UHFLI-QC. UHFLI-QC includes an internal arbitrary waveform generator (AWG), logging units (log), timetrace averager (AVG), and complex weighted integration units. The amplification chain includes a high-electron-mobility transistor (HEMT), intermediate-frequency (IF), low-noise (LN), and ultralow-noise (ULN) amplifiers.

tone for the TWPA is generated at room temperature and combined with the signal using a directional coupler at the TWPA input. After the isolator, the signal is also bandpass filtered at the base temperature followed by further amplification with a high-electron-mobility transistor (HEMT) amplifier at the 4-K stage and ultralow-noise (ULN) and a low-noise (LN) amplifier at room temperature. The signal is then down-converted using the same local oscillator (LO) as used for up-conversion. Before digitization, the intermediate-frequency (IF) signal is again amplified, to make optimal use of the dynamic range of the UHFLI. The warm amplification (WAMP) and down-conversion (DC) boards feature attenuation and additional filters to suppress standing waves and noise outside the detection band.

We further process the digitized signal, by using the internal signal-processing-unit functionalities of the UHFLI. For data shown in Fig. 4, we average signal time traces over several trigger events. For single-shot measurements, we perform several weighted integrations in parallel, each with different integration weights, and record the individual results.

The qubit drive pulses are generated using a channel pair of an AWG at 1.2 gigasamples per second. The qubit drive lines have the same cold attenuator configuration as the probe tone input. To tune the qubit frequencies, we apply current bias by controlling the voltage across a bias resistor. At 100- and 12-mK temperature stages, the flux line signals are low-pass filtered with a cutoff at 1 GHz. The flux lines are also equipped with EccoSorb filters at the base temperature to suppress noise above 15 GHz.

APPENDIX B: DETAILED SAMPLE DESCRIPTION

To determine characteristic qubit parameters of our device, Table III, we use standard spectroscopy and time-resolved measurement techniques. We measure the exact qubit frequencies and T_2^* using a standard Ramsey protocol. The anharmonicity is extracted from a spectroscopic measurement of the two-photon transition into the second excited state. The qubit energy relaxation time T_1 is characterized by standard time-domain experiments. We determine the thermal population of the excited state P_{therm} from the probability that the qubit is found to be in the excited state in the preselection readout conducted before every single-shot experiment run. For all single-qubit gates, we used DRAG-shaped [49] π pulses with length $2.5\sigma = 50$ ns. Qubit Q5 exhibited significant frequency instability and as indicated in Table III we use it in a different configuration for the measurement discussed in Sec. V.

Parameters of the readout resonators and Purcell filters are extracted from the feedline transmission spectroscopy fits, as discussed in Sec. III. We chose the intermediate frequencies of the probe pulses $\nu_{\text{RO mod}}$ such that the second sideband of the upconversion process would not

overlap with the untargeted readout resonator frequencies. The photon number during the readout n_{RO} is measured using an ac Stark shift measurement and the critical photon number $n_{\text{crit}} = g^2/[4(\omega_Q - \omega_R)^2]$ is calculated from the parameters of the readout circuit [40].

The device is fabricated on a substrate of *c*-plane-cut single-side-polished sapphire from Rubicon Technology. A 150-nm thin niobium film was deposited by STAR Cryoelectronics on wafers cleaned by acetone and IPA in an ultrasonic bath at 50°C. The circuit, except the Josephson junctions, is defined by optical lithography and dry-etching process. Josephson junctions are formed by Al/AIO_x/Al layers deposited in an electron-beam Plassys evaporator with a Dolan bridge shadow evaporation technique. Native Nb oxide is removed using ion milling before and after defining the electron-beam mask.

APPENDIX C: INPUT-OUTPUT THEORY

As discussed in the main text, the feedline of the sample is capacitively coupled to the input port. Here, we calculate the scattering parameters in the presence of the input capacitor using input-output formalism [50,51], also known as coupled mode theory [52,53], in order to model the transmission spectrum from port 1 to port 2, as shown in Fig. 9.

The equations of motion for the coupled Purcell filter mode *a* and readout resonator mode *b* is given as

$$\frac{da}{dt} = -i\Delta_a a - \frac{\kappa_a + \gamma_a}{2} a - iJb + \sqrt{\kappa_a} a_i, \quad (\text{C1a})$$

$$\frac{db}{dt} = -i\Delta_b b - \frac{\kappa_b + \gamma_b}{2} b - iJa + \sqrt{\kappa_b} b_i, \quad (\text{C1b})$$

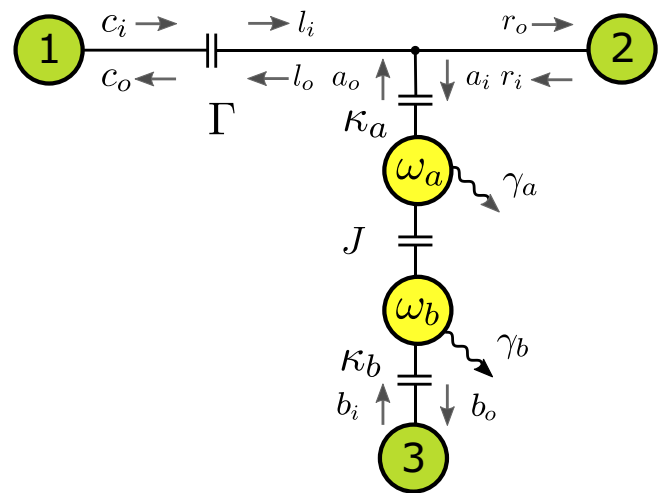


FIG. 9. Input-output network of the readout circuit including feedline, Purcell filter, and readout resonator with input and output ports (green circles), resonator modes (yellow circles), traveling mode amplitudes (arrows), dissipation channels (wiggly arrows), and capacitive couplings of the elements.

where $\Delta_{\{a,b\}} = \omega_{\{a,b\}} - \omega_d$ is the detuning between the drive frequency of the input field ω_d and the bare resonance frequency $\omega_{a,b}$ of the respective mode, J is the coupling strength of the modes a and b , and the rates γ_a and γ_b are the nonradiative internal loss rates of the resonators. The corresponding input-output relations are

$$a_o = a_i - \sqrt{\kappa_a}a, \quad (\text{C2a})$$

$$b_o = b_i - \sqrt{\kappa_b}b, \quad (\text{C2b})$$

where direction of the input (i) and output (o) modes is indicated in Fig. 9, κ_a is the coupling rate between the Purcell filter and the feedline and κ_b is the coupling rate between the readout resonator and the qubit drive line.

The t junction connecting the Purcell filter (a) with the right (r) and left (l) side of the feedline is energy conserving, reciprocal, and symmetric. Therefore, the scattering matrix describing the t junction is unitary and symmetric [54] and obeys $S_{12} = S_{23} = S_{31}$. Up to a sign convention, the only such scattering matrix corresponds to the relations

$$l_o = -\frac{1}{3}l_i + \frac{2}{3}r_i + \frac{2}{3}a_o, \quad (\text{C3})$$

$$r_o = \frac{2}{3}l_i - \frac{1}{3}r_i + \frac{2}{3}a_o, \quad (\text{C4})$$

$$a_i = \frac{2}{3}l_i + \frac{2}{3}r_i - \frac{1}{3}a_o \quad (\text{C5})$$

where a_i, b_i, c_i and a_o, b_o, c_o are input and output modes of the three corresponding ports with respect to the Purcell filter. The input capacitor is described by the scattering relations [54]

$$c_o = (1 - \Gamma)l_o + \Gamma c_i \quad (\text{C6a})$$

$$l_i = (1 - \Gamma)c_i + \Gamma l_o, \quad (\text{C6b})$$

where $\Gamma(\omega) = 1/(1 + 2i\omega Z_0 C_{\text{in}})$ with characteristic impedance Z_0 and capacitance C_{in} of the input capacitor.

Combining all the input-output relations and assuming a negligible dispersion between the t junction and the input capacitor, we eliminate modes l and a such that the equations of motion become

$$\begin{aligned} \frac{da}{dt} &= -i\tilde{\Delta}_a a - \frac{\tilde{\kappa}_a + \gamma_a}{2}a - iJb \\ &+ \frac{\sqrt{\kappa_a}}{2}[(1 - \Gamma)c_i + (1 + \Gamma)r_i], \end{aligned} \quad (\text{C7a})$$

$$\frac{db}{dt} = -i\Delta_b b - \frac{\kappa_b + \gamma_b}{2}b - iJa + \sqrt{\kappa_b}b_i \quad (\text{C7b})$$

with effective linewidth

$$\tilde{\kappa}_a = \kappa_a \frac{1 + \text{Re}\{\Gamma\}}{2} \quad (\text{C8})$$

and effective frequency

$$\tilde{\omega}_a = \omega_a + \kappa_a \frac{\text{Im}\{\Gamma\}}{4}. \quad (\text{C9})$$

In the limit $\Gamma \rightarrow 1$ for which the Purcell filter is coupled only to a single port $\tilde{\kappa}_a \rightarrow \kappa_a$ and $\tilde{\omega}_a \rightarrow \omega_a$. The input-output relations corresponding to the above equations of motion now read

$$c_o = c_i + (1 - \Gamma)r_i - \frac{\sqrt{\kappa_a}}{2}(1 - \Gamma)a, \quad (\text{C10a})$$

$$r_o = r_i + (1 - \Gamma)c_i - \frac{\sqrt{\kappa_a}}{2}(1 + \Gamma)a, \quad (\text{C10b})$$

$$b_o = b_i - \sqrt{\kappa_b}b. \quad (\text{C10c})$$

To extract the scattering parameters of the system, we solve Eq. (C7) for the steady state ($da/dt = db/dt = 0$) and substitute the solution into Eqs. (C10). By setting $r_i = b_i = 0$, this approach yields the transmission coefficient through the feedline

$$\begin{aligned} \frac{S_{21}}{1 - \Gamma} &= \frac{r_o/c_i}{1 - \Gamma} = 1 - \frac{1 + \Gamma}{1 + \text{Re}\{\Gamma\}} \\ &\times \frac{\tilde{\kappa}_a(\gamma_b + 2i\Delta_b + \kappa_b)}{4J^2 + (\gamma_a + 2i\tilde{\Delta}_a + \tilde{\kappa}_a)(\gamma_b + 2i\Delta_b + \kappa_b)}, \end{aligned} \quad (\text{C11})$$

normalized by the insertion loss induced by the input coupler of the feedline. Equation (C11) is the model we used to fit to the data in Fig. 3(b). To obtain the transmission coefficient from the weakly coupled qubit drive line to the output port of the transmission line we set $r_i = c_i = 0$:

$$\begin{aligned} S_{23} &= \frac{r_o}{b_i} = \frac{1 + \Gamma}{\sqrt{2}(1 + \text{Re}\{\Gamma\})} \\ &\times \frac{4iJ\sqrt{\kappa_a}\sqrt{\kappa_b}}{4J^2 + (\gamma_a + 2i\tilde{\Delta}_a + \tilde{\kappa}_a)(\gamma_b + 2i\Delta_b + \kappa_b)}, \end{aligned} \quad (\text{C12})$$

which describes the data shown in Fig. 3(a).

To extract the exact expression for κ_R [39], we rewrite Eq. (C7) in a matrix form and find the eigenvalues in the steady state and without external drive. The real part of the eigenvalues are the effective linewidth of the corresponding modes. We approximate $\gamma_{a,b}, \kappa_b \approx 0$ and thus the effective linewidth of the readout resonators becomes

$$\kappa_R = \frac{1}{2} \left(\tilde{\kappa}_a - \text{Re} \left\{ \sqrt{-16J^2 + (\tilde{\kappa}_a - 2i\tilde{\Delta}_{ab})^2} \right\} \right), \quad (\text{C13})$$

which is the expression used to calculate the readout resonator linewidth in Table I from the fitted parameters. In the main text, we denote the Purcell resonator frequency $\tilde{\omega}_a = \omega_P$ and the linewidth $\tilde{\kappa}_a = \kappa_P$.

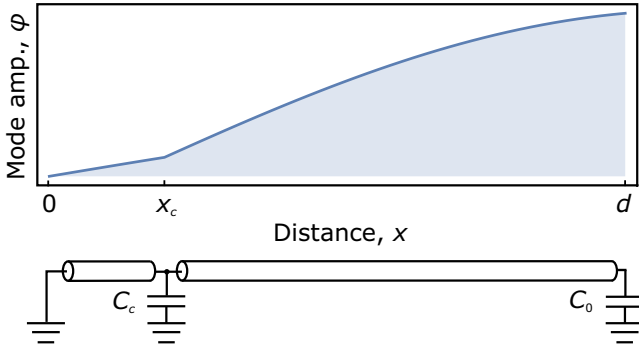


FIG. 10. Mode function and circuit model for the $\lambda/4$ resonator with capacitances C_0 and C_c to ground at distances d and x_c from the terminated end, respectively.

APPENDIX D: CALCULATING THE RESONATOR FREQUENCIES

We realize both the Purcell filters and the readout resonators as a transmission-line-based $\lambda/4$ resonator. We model each resonator with the circuit shown in Fig. 10 consisting of a transmission line of length d grounded at $x = 0$, coupled to ground at $x = x_c$ and $x = x_d$ with capacitance C_c and C_0 accordingly. Here, we consider all elements coupled to the studied resonator to be effectively grounded and thus the capacitances C_c and C_0 include both the coupling to the ground and to the other circuit element.

The field amplitude along the transmission line on both sides of the coupling at x_c is described by the standard wave equation. Thus, the mode function for the flux variable $\phi(x, t)$ (time integral of the voltage) of each resonator is given by [55]

$$\phi(x, t) = \phi_0 \sin(\omega t) \times \begin{cases} B \sin(kx) & \text{for } 0 \leq x \leq x_c, \\ \cos[k(x - d) - \theta] & \text{for } x_c \leq x \leq d, \end{cases} \quad (\text{D1})$$

with the mode amplitude ϕ_0 , unitless scaling factor B , phase offset θ , wave number $k = \omega/v$, and resonance frequency ω . Moreover, $v = 1/\sqrt{lc}$ is the phase velocity of field with inductance l and capacitance c per unit length of the resonator. Since the mode at $x = x_c$ has to be continuous, the scaling factor becomes

$$B = \frac{\cos[k(x_c - d) - \theta]}{\sin(kx_c)}. \quad (\text{D2})$$

There are three boundary conditions due to the grounded end and extra capacitors. The boundary condition at the terminated end is fulfilled directly by the choice of the mode function. The other two boundary conditions are

set by Kirchoff's law for current derived from the Euler-Lagrange equation [51,55]

$$\ddot{\phi}(d, t) + \frac{1}{C_0 l} \frac{\partial}{\partial x} \phi(x, t) \Big|_{x=d} = 0, \quad (\text{D3})$$

$$\ddot{\phi}(x_c, t) + \frac{1}{C_c l} \left[\frac{\partial}{\partial x} \phi(x, t) \Big|_{x=x_{c+}} - \frac{\partial}{\partial x} \phi(x, t) \Big|_{x=x_{c-}} \right] = 0. \quad (\text{D4})$$

When inserting Eq. (D1) into Eqs. (D3) and (D4), we obtain the following result:

$$\tan(\theta) = C_0 Z_0 \omega, \quad (\text{D5})$$

$$\tan(kx_c)^{-1} + \tan[k(x_c - d) - \theta] = C_c Z_0 \omega, \quad (\text{D6})$$

where $Z_0 = \sqrt{l/c}$ is the characteristic impedance of the coplanar waveguide.

We solve Eqs. (D5) and (D6) numerically to find ω and θ for a given resonator length, and C_0 and C_c obtained from finite-element simulations. Typical values for the capacitances are $C_c = 6.5$ fF between the Purcell filter and readout resonator, $C_0 = 61.3$ fF between the qubit and readout resonator, and $C_0 = 45\text{--}60$ fF between the Purcell filter and feedline. These additional capacitances result in a typical resonance frequency shift of 600–700 MHz. Using these solutions we can accurately predict the frequency of each resonator, which ensures that the readout resonators are on resonance with its Purcell filters and that we achieve equidistant frequency spacing between the resonators of the different qubits.

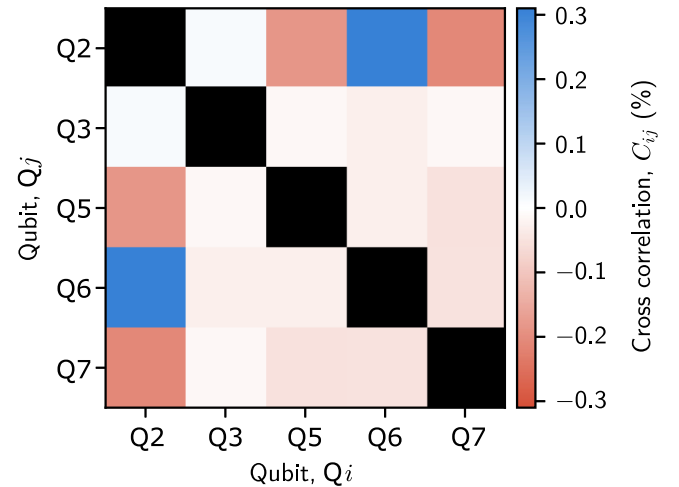


FIG. 11. Correlation coefficients between the outcomes of the multiplexed single-shot measurements as calculated by Eq. (E1).

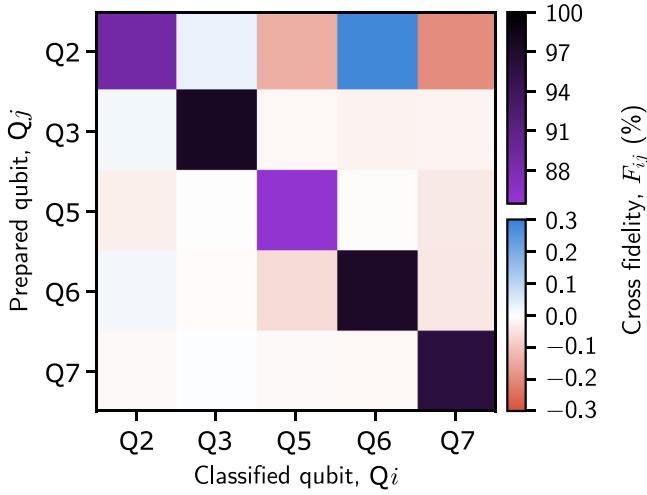


FIG. 12. Cross fidelity calculated using Eq. (E2). The diagonal elements correspond to the single-qubit readout fidelities.

APPENDIX E: CORRELATIONS AND CROSS-ASSIGNMENT FIDELITY

Correlations in the qubit-state assignment can result from a variety of mechanisms such as finite cross couplings on the device, the spectral overlap of individual readout signals and detection bands of different qubits, and nonlinearities in the amplification chain. Here we discuss two metrics, which can be used to benchmark such imperfections: Cross correlation, which describes the correlation between the assigned states, and cross fidelity, which assesses correlations between the prepared and assigned states. We extract both quantities from the assignment probability matrix presented in Fig. 6.

The correlations in the state assignment of a pair of qubits \$Q_i\$ and \$Q_j\$ are quantified by a cross-correlation matrix

$$C_{ij} = \frac{\text{cov}(\sigma_{zi}, \sigma_{zj})}{\sqrt{\text{var}(\sigma_{zi}) \text{var}(\sigma_{zj})}}, \quad (\text{E1})$$

where the covariance cov and variance var are taken over all prepared states and states assigned to other qubits. Ideally, we expect no cross correlations \$C_{ij} = 0\$ (\$i \neq j\$) while the diagonal elements \$C_{ii} = 1\$ by definition. The cross-correlation matrix shown in Fig. 11 is extracted from the experimental data and shows finite off-diagonal elements, which, however, are small compared to the single-qubit measurement-error probabilities discussed in the main text.

Correlations between the assigned and prepared states are described by the cross fidelity

$$F_{ij} = 1 - P(e_i|0_j) - P(g_i|\pi_j), \quad (\text{E2})$$

where the probability \$P\$ is taken over the assignment (preparation) of all qubits but \$i\$ (\$j\$). Ideally, the readout

TABLE IV. Measurement efficiency for each qubit calculated by Eq. (F2) from a Ramsey-type measurement discussed in the main text.

	Q2	Q3	Q5	Q6	Q7
Efficiency, \$\eta\$	51.8%	49.9%	42.7%	51.2%	47.9%

result of \$Q_i\$ should be uncorrelated with the preparation of \$Q_j\$ and we expect \$P(e_i|0_j) = P(g_i|\pi_j) = 0.5\$ and, thus, the off-diagonal elements should be 0. The measured matrix \$F_{ij}\$ in Fig. 12 shows small off-diagonal elements approximately 0.3% compared to the single qubit errors approximately 3%.

APPENDIX F: MEASUREMENT EFFICIENCY

We extract the total measurement efficiency from a comparison between the measurement-induced dephasing and the signal-to-noise-ratio (SNR). The quantum-limited SNR for dispersive readout with a phase-preserving amplifier and lossless detection chain is given by [44]

$$\text{SNR}_{\text{QL}}^2 = 4\bar{\Gamma}_{ii}\tau_p, \quad (\text{F1})$$

where \$\tau_p\$ is the measurement pulse length and \$\bar{\Gamma}_{ii}\$ is the average measurement-induced dephasing rate obtained from the Ramsey-type experiment described in Sec. V. We extract the SNR from the histograms of single-shot measurement signals as described in Sec. IV. and define the measurement efficiency of the whole detection chain for a qubit \$Q_i\$ as

$$\eta_i = \frac{\text{SNR}^2}{\text{SNR}_{\text{QL}}^2} = \frac{\text{SNR}^2}{4\bar{\Gamma}_{ii}\tau_p}. \quad (\text{F2})$$

The observed measurement efficiencies are in the range of 42% to 52% as listed in Table IV. The measurement efficiency is mostly limited by the internal loss in the TWPA [26] and in the MW components between the sample and TWPA. We attribute variations of the measurement efficiency for the different measured qubits mostly to the frequency-dependent gain of the TWPA.

[1] M. A. Nielsen and Isaac L. Chuang, Programmable Quantum Gate Arrays, *Phys. Rev. Lett.* **79**, 321 (1997).
 [2] David P. DiVincenzo, Fault-tolerant architectures for superconducting qubits, *Phys. Scr.* **2009**, 014020 (2009).
 [3] R. Barends *et al.* Superconducting quantum circuits at the surface code threshold for fault tolerance, *Nature* **508**, 500 (2014).
 [4] Charles H. Bennett, Gilles Brassard, Claude Crépeau, Richard Jozsa, Asher Peres, and William K. Wootters, Teleporting an Unknown Quantum State via Dual Classical and Einstein-Podolsky-Rosenchannels, *Phys. Rev. Lett.* **70**, 1895 (1993).

- [5] L. Steffen, Y. Salathe, M. Oppliger, P. Kurpiers, M. Baur, C. Lang, C. Eichler, G. Puebla-Hellmann, A. Fedorov, and A. Wallraff, Deterministic quantum teleportation with feed-forward in a solid state system, *Nature* **500**, 319 (2013).
- [6] J. E. Johnson, C. Macklin, D. H. Slichter, R. Vijay, E. B. Weingarten, John Clarke, and I. Siddiqi, Heralded State Preparation in a Superconducting Qubit, *Phys. Rev. Lett.* **109**, 050506 (2012).
- [7] D. Ristè, J. G. van Leeuwen, H.-S. Ku, K. W. Lehnert, and L. DiCarlo, Initialization by Measurement of a Superconducting Quantum Bit Circuit, *Phys. Rev. Lett.* **109**, 050507 (2012).
- [8] Yves Salathé, Philipp Kurpiers, Thomas Karg, Christian Lang, Christian Kraglund Andersen, Abdulkadir Akin, Sebastian Krinner, Christopher Eichler, and Andreas Wallraff, Low-latency Digital Signal Processing for Feedback and Feed Forward in Quantum Computing and Communication, *Phys. Rev. Applied* **9**, 034011 (2018).
- [9] M. Jerger, S. Poletto, P. Macha, U. Hübner, E. Il'ichev, and A. V. Ustinov, Frequency division multiplexing readout and simultaneous manipulation of an array of flux qubits, *Appl. Phys. Lett.* **101**, 042604 (2012).
- [10] V. Schmitt, X. Zhou, K. Juliusson, B. Royer, A. Blais, P. Bertet, D. Vion, and D. Esteve, Multiplexed readout of transmon qubits with Josephson bifurcation amplifiers, *Phys. Rev. A* **90**, 062333 (2014).
- [11] E. Jeffrey, D. Sank, J. Y. Mutus, T. C. White, J. Kelly, R. Barends, Y. Chen, Z. Chen, B. Chiaro, A. Dunsworth, A. Megrant, P. J. J. O'Malley, C. Neill, P. Roushan, A. Vainsencher, J. Wenner, A. N. Cleland, and J. M. Martinis, Fast Accurate State Measurement with Superconducting Qubits, *Phys. Rev. Lett.* **112**, 190504 (2014).
- [12] Alexandre Blais, Ren-Shou Huang, Andreas Wallraff, S. M. Girvin, and R. J. Schoelkopf, Cavity quantum electrodynamics for superconducting electrical circuits: An architecture for quantum computation, *Phys. Rev. A* **69**, 062320 (2004).
- [13] A. Wallraff, D. I. Schuster, A. Blais, L. Frunzio, J. Majer, M. H. Devoret, S. M. Girvin, and R. J. Schoelkopf, Approaching Unit Visibility for Control of a Superconducting Qubit with Dispersive Readout, *Phys. Rev. Lett.* **95**, 060501 (2005).
- [14] C. M. Caves, Quantum limits on noise in linear amplifiers, *Phys. Rev. D* **26**, 1817 (1982).
- [15] B. Yurke, M. L. Roukes, R. Movshovich, and A. N. Pargellis, A low-noise series-array Josephson junction parametric amplifier, *Appl. Phys. Lett.* **69**, 3078 (1996).
- [16] M. A. Castellanos-Beltran, K. D. Irwin, G. C. Hilton, L. R. Vale, and K. W. Lehnert, Amplification and squeezing of quantum noise with a tunable Josephson metamaterial, *Nat. Phys.* **4**, 929 (2008).
- [17] C. Eichler, Y. Salathe, J. Mlynek, S. Schmidt, and A. Wallraff, Quantum-limited Amplification and Entanglement in Coupled Nonlinear Resonators, *Phys. Rev. Lett.* **113**, 110502 (2014).
- [18] Francois Mallet, Florian R. Ong, Agustin Palacios-Laloy, Francois Nguyen, Patrice Bertet, Denis Vion, and Daniel Esteve, Single-shot qubit readout in circuit quantum electrodynamics, *Nat. Phys.* **5**, 791 (2009).
- [19] R. Vijay, D. H. Slichter, and I. Siddiqi, Observation of Quantum Jumps in a Superconducting Artificial Atom, *Phys. Rev. Lett.* **106**, 110502 (2011).
- [20] M. D. Reed, B. R. Johnson, A. A. Houck, L. DiCarlo, J. M. Chow, D. I. Schuster, L. Frunzio, and R. J. Schoelkopf, Fast reset and suppressing spontaneous emission of a superconducting qubit, *Appl. Phys. Lett.* **96**, 203110 (2010).
- [21] Nicholas T. Bronn, Yanbing Liu, Jared B. Hertzberg, Antonio D. Córcoles, Andrew A. Houck, Jay M. Gambetta, and Jerry M. Chow, Broadband filters for abatement of spontaneous emission in circuit quantum electrodynamics, *Appl. Phys. Lett.* **107**, 172601 (2015).
- [22] T. Walter, P. Kurpiers, S. Gasparinetti, P. Magnard, A. Potocnik, Y. Salathé, M. Pechal, M. Mondal, M. Oppliger, C. Eichler, and A. Wallraff, Rapid, High-fidelity, Single-shot Dispersive Readout of Superconducting Qubits, *Phys. Rev. Applied* **7**, 054020 (2017).
- [23] S. Filipp, P. Maurer, P. J. Leek, M. Baur, R. Bianchetti, J. M. Fink, M. Göppl, L. Steffen, J. M. Gambetta, A. Blais, and A. Wallraff, Two-qubit State Tomography using a Joint Dispersive Readout, *Phys. Rev. Lett.* **102**, 200402 (2009).
- [24] L. DiCarlo, M. D. Reed, L. Sun, B. R. Johnson, J. M. Chow, J. M. Gambetta, L. Frunzio, S. M. Girvin, M. H. Devoret, and R. J. Schoelkopf, Preparation and measurement of three-qubit entanglement in a superconducting circuit, *Nature* **467**, 574 (2010).
- [25] J. Y. Mutus, T. C. White, R. Barends, Yu Chen, Z. Chen, B. Chiaro, A. Dunsworth, E. Jeffrey, J. Kelly, A. Megrant, C. Neill, P. J. J. O'Malley, P. Roushan, D. Sank, A. Vainsencher, J. Wenner, K. M. Sundqvist, A. N. Cleland, and John M. Martinis, Strong environmental coupling in a Josephson parametric amplifier, *Appl. Phys. Lett.* **104**, 263513 (2014).
- [26] C. Macklin, K. O'Brien, D. Hover, M. E. Schwartz, V. Bolkhovskoy, X. Zhang, W. D. Oliver, and I. Siddiqi, A near-quantum-limited Josephson traveling-wave parametric amplifier, *Science* **350**, 307 (2015).
- [27] Tanay Roy, Suman Kundu, Madhavi Chand, A. M. Vadiraj, A. Ranadive, N. Nehra, Meghan P. Patankar, J. Aumentado, A. A. Clerk, and R. Vijay, Broadband parametric amplification with impedance engineering: Beyond the gain-bandwidth product, *Appl. Phys. Lett.* **107**, 262601 (2015).
- [28] C. Neill *et al.*, A blueprint for demonstrating quantum supremacy with superconducting qubits, *Science* **360**, 195 (2018), <http://science.sciencemag.org/content/360/6385/195.full.pdf>.
- [29] A. D. Corcoles, Easwar Magesan, Srikanth J. Srinivasan, Andrew W. Cross, M. Steffen, Jay M. Gambetta, and Jerry M. Chow, Demonstration of a quantum error detection code using a square lattice of four superconducting qubits, *Nat. Commun.* **6**, 6979 (2015).
- [30] Matthew Reagor *et al.*, Demonstration of universal parametric entangling gates on a multi-qubit lattice, *Sci. Adv.* **4**, eaao3603 (2018).
- [31] C. C. Bultink, M. A. Rol, T. E. O'Brien, X. Fu, B. C. S. Dikken, C. Dickel, R. F. L. Vermeulen, J. C. de Sterke, A. Bruno, R. N. Schouten, and L. DiCarlo, Active Resonator

- Reset in the Nonlinear Dispersive Regime of Circuit QED, *Phys. Rev. Applied* **6**, 034008 (2016).
- [32] Serwan Asaad, Christian Dickel, Nathan K. Langford, Stefano Poletto, Alessandro Bruno, Michiel Adriaan Rol, Duije Deurloo, and Leonardo DiCarlo, Independent, extensible control of same-frequency superconducting qubits by selective broadcasting, *npj Quantum Inf.* **2**, 16029 (2016).
- [33] Chao Song, Kai Xu, Wuxin Liu, Chui-ping Yang, Shi-Biao Zheng, Hui Deng, Qiwei Xie, Keqiang Huang, Qiujiang Guo, Libo Zhang, Pengfei Zhang, Da Xu, Dongning Zheng, Xiaobo Zhu, H. Wang, Y.-A. Chen, C.-Y. Lu, Siyuan Han, and Jian-Wei Pan, 10-qubit Entanglement and Parallel Logic Operations with a Superconducting Circuit, *Phys. Rev. Lett.* **119**, 180511 (2017).
- [34] N. T. Bronn, B. Abdo, K. Inoue, S. Lekuch, A. D. Córcoles, J. B. Hertzberg, M. Takita, L. S. Bishop, J. M. Gambetta, and J. M. Chow, Fast, high-fidelity readout of multiple qubits, *J. Phys. Conf. Ser.* **834**, 012003 (2017).
- [35] Austin G. Fowler, Matteo Mariantoni, John M. Martinis, and Andrew N. Cleland, Surface codes: Towards practical large-scale quantum computation, *Phys. Rev. A* **86**, 032324 (2012).
- [36] Robert B. Griffiths and Chi-Sheng Niu, Semiclassical Fourier Transform for Quantum Computation, *Phys. Rev. Lett.* **76**, 3228 (1996).
- [37] Charles H. Bennett, Gilles Brassard, Sandu Popescu, Benjamin Schumacher, John A. Smolin, and William K. Wootters, Purification of Noisy Entanglement and Faithful Teleportation via Noisy Channels, *Phys. Rev. Lett.* **76**, 722 (1996).
- [38] Bernard Yurke and David Stoler, Bell's-inequality experiments using independent-particle sources, *Phys. Rev. A* **46**, 2229 (1992).
- [39] E. A. Sete, J. M. Martinis, and A. N. Korotkov, Quantum theory of a bandpass purcell filter for qubit readout, *Phys. Rev. A* **92**, 012325 (2015).
- [40] J. Gambetta, A. Blais, D. I. Schuster, A. Wallraff, L. Frunzio, J. Majer, M. H. Devoret, S. M. Girvin, and R. J. Schoelkopf, Qubit-photon interactions in a cavity: Measurement-induced dephasing and number splitting, *Phys. Rev. A* **74**, 042318 (2006).
- [41] J. Koch, T. M. Yu, J. Gambetta, A. A. Houck, D. I. Schuster, J. Majer, A. Blais, M. H. Devoret, S. M. Girvin, and R. J. Schoelkopf, Charge-insensitive qubit design derived from the Cooper pair box, *Phys. Rev. A* **76**, 042319 (2007).
- [42] R. Barends, J. Kelly, A. Megrant, D. Sank, E. Jeffrey, Y. Chen, Y. Yin, B. Chiaro, J. Mutus, C. Neill, P. O'Malley, P. Roushan, J. Wenner, T. C. White, A. N. Cleland, and John M. Martinis, Coherent Josephson Qubit Suitable for Scalable Quantum Integrated Circuits, *Phys. Rev. Lett.* **111**, 080502 (2013).
- [43] J. Gambetta, W. A. Braff, A. Wallraff, S. M. Girvin, and R. J. Schoelkopf, Protocols for optimal readout of qubits using a continuous quantum nondemolition measurement, *Phys. Rev. A* **76**, 012325 (2007).
- [44] C. C. Bultink, B. Tarasinski, N. Haandbk, S. Poletto, N. Haider, D. J. Michalak, A. Bruno, and L. DiCarlo, General method for extracting the quantum efficiency of dispersive qubit readout in circuit QED, *Appl. Phys. Lett.* **112**, 092601 (2018).
- [45] X. Y. Jin, A. Kamal, A. P. Sears, T. Gudmundsen, D. Hover, J. Miloshi, R. Slattery, F. Yan, J. Yoder, T. P. Orlando, S. Gustavsson, and W. D. Oliver, Thermal and Residual Excited-state Population in a 3D Transmon Qubit, *Phys. Rev. Lett.* **114**, 240501 (2015).
- [46] Maxime Boissonneault, J. M. Gambetta, and Alexandre Blais, Dispersive regime of circuit QED: Photon-dependent qubit dephasing and relaxation rates, *Phys. Rev. A* **79**, 013819 (2009).
- [47] D. H. Slichter, R. Vijay, S. J. Weber, S. Boutin, M. Boissonneault, J. M. Gambetta, A. Blais, and I. Siddiqi, Measurement-induced Qubit State Mixing in Circuit QED from Up-converted Dephasing Noise, *Phys. Rev. Lett.* **109**, 153601 (2012).
- [48] R. Versluis, S. Poletto, N. Khammassi, B. Tarasinski, N. Haider, D. J. Michalak, A. Bruno, K. Bertels, and L. DiCarlo, Scalable Quantum Circuit and Control for a Superconducting Surface Code, *Phys. Rev. Applied* **8**, 034021 (2017).
- [49] F. Motzoi, J. M. Gambetta, P. Rebentrost, and F. K. Wilhelm, Simple Pulses for Elimination of Leakage in Weakly Nonlinear Qubits, *Phys. Rev. Lett.* **103**, 110501 (2009).
- [50] C. W. Gardiner and M. J. Collett, Input and output in damped quantum systems: Quantum stochastic differential equations and the master equation, *Phys. Rev. A* **31**, 3761 (1985).
- [51] Bernard Yurke and John S. Denker, Quantum network theory, *Phys. Rev. A* **29**, 1419 (1984).
- [52] A. Yariv, Coupled-mode theory for guided-wave optics, *IEEE J. Quantum Electron.* **9**, 919 (1973).
- [53] H. A. Haus and W. Huang, Coupled-mode theory, *Proc. IEEE* **79**, 1505 (1991).
- [54] D. M. Pozar, *Microwave Engineering* (Wiley & Sons, Inc., New Jersey, USA, 2012), 4th ed.
- [55] J. Bourassa, F. Beaudoin, Jay M. Gambetta, and A. Blais, Josephson-junction-embedded transmission-line resonators: From Kerr medium to in-line transmon, *Phys. Rev. A* **86**, 013814 (2012).